Carbon 176 (2021) 431–439

Contents lists available at ScienceDirect

Carbon

journal homepage: www.elsevier.com/locate/carbon

Twisted graphene in graphite: Impact on surface potential and chemical stability

Tuan-Hoang Tran [a], Raul D. Rodriguez [a, *], Marco Salerno [b, c], Aleksandar Matković [d], Christian Teichert [d], Evgeniya Sheremet [a, **]

[a] Tomsk Polytechnic University, Lenina ave. 30, 634034, Tomsk, Russia
[b] Istituto Italiano di Tecnologia, Via Morego 30, 16163, Genova, Italy
[c] Department of Functional Materials and Hydrogen Technology, Military University of Technology, 2 Kaliskiego Str., 00-908, Warsaw, Poland
[d] Institute of Physics, Montanuniversität Leoben, Franz Josef Strasse 18, 8700, Leoben, Austria

ARTICLE INFO

Article history:
Received 3 November 2020
Received in revised form
10 January 2021
Accepted 30 January 2021
Available online 5 February 2021

Keywords:
Graphene
Graphite
Moiré pattern
Twisted bi-layers
Kelvin probe force microscopy
Surface potential
Contact potential difference
HOPG
Surface contamination
Raman spectroscopy

ABSTRACT

Highly-oriented pyrolytic graphite (HOPG), *i.e.*, the 3D stack of sp^2-hybridized carbon sheets, is an attractive material thanks to its high electrical conductivity, chemical inertness, thermal stability, atomic-scale flatness, and ease of exfoliation. Despite an apparently ideal and uniform material, freshly cleaved HOPG shows domains in Kelvin probe force microscopy (KPFM) with surface potential contrast over 30 mV. We systematically investigated these domains using an integrated approach, including time-dependent KPFM and hyperspectral Raman imaging. The observed time-evolving domains are attributed to locally different hydrocarbon adsorption from the environment, driven by structural defects likely related to rotational mismatch, *i.e.*, twisted layers. These defects affect the interlayer coupling between topmost graphene and the underlying layers. Our hypothesis was supported by Raman spectroscopy results, showing domains with G peak shifts and 2D line shape compatible with bilayer graphene. We attribute the selective sensitivity of our Raman spectroscopy results to the top graphene layers as resonances due to van Hove singularities. Our results show that the chemical and electrical properties of HOPG are far more complex than what is generally believed due to the broken symmetry at the top surface, giving rise to graphene bilayer-like behavior.

1. Introduction

Since the isolation of single-layer graphene from the atomic layers of highly oriented pyrolytic graphite (HOPG) in 2004 [1], graphene and related van der Waals materials like MoS_2 [2] and GaSe [3] are gaining considerable interest in the scientific community. HOPG comes in different grades of quality and is inexpensive, atomically flat, and smooth. It is known that HOPG can be readily obtained as a clean surface, free of contaminants, by the mechanical removal of the topmost layers with adhesive tape that makes it an excellent reference material for scanning probe microscopy methods. This is one reason why HOPG is so attractive in fundamental research for investigating a wide range of systems, from chemical to biological [4–8]. For example, atomic-resolution imaging of HOPG is one of the basic tests for scanner calibration and tip spatial resolution in scanning tunneling microscopy (STM) [9]. Beyond topography applications, HOPG is also used to quantify other material properties like the probe's work function and an arbitrary sample deposited on HOPG analyzed by Kelvin probe force microscopy (KPFM) [10]. For this application, HOPG is usually preferred to gold, since gold has to be annealed to obtain crystalline flat planes, which additionally are limited to a smaller lateral linear size of the order of 100 nm. In the case of deposited gold, either by evaporation or sputter deposition, the surface roughness induces differences in work function and the values with respect to Au(111) can vary as much as 1 eV [11,12]. From the electrical point of view, HOPG is also superior to Si, which forms a native insulating oxide layer under ambient conditions.

An idealized HOPG can be considered as a vertical stacking of identical graphene layers held together by van der Waals forces. Consequently, one expects to see a homogeneous electrical surface potential (SP) distribution on HOPG with no spatial heterogeneities

* Corresponding author.
** Corresponding author.
E-mail address: esheremet@tpu.ru (R.D. Rodriguez).

https://doi.org/10.1016/j.carbon.2021.01.152

beyond quasi-one-dimensional features at the grain boundaries [13]. However, the SP local heterogeneity of HOPG was reported before [14]. Proksch observed similar image contrast domains on HOPG - apparently connected to the layered texture - by mechanical measurements with bi-modal amplitude-modulated atomic force microscopy (AFM) [15], and proposed that these regions arise due to local adsorption of water from the air. He also observed the growth of these regions over time. In contrast, based on electric force microscopy, Lu *et al.* [16] interpreted the image contrast as a purely electrical effect, arising due to the lack of local interlayer conductivity in HOPG that induces a buildup of static charge. They argued that this effect occurs in some domains where the top graphene layer of HOPG is electrically decoupled from the lower layers, in contrast to most of the surface where there is an electrical connection among graphene layers. Lu *et al.* claimed to rule out water or other surface contaminants' effects by performing the measurements in the Ar atmosphere. Sadewasser and Glatzel [17] commented on Lu's work, and the response to that comment [18] opened a debate on whether the spatial heterogeneities are the result of contaminant adsorption from the environment or they are intrinsic to HOPG.

In this work, we used a complementary approach with Raman hyperspectral imaging and KPFM implemented on instruments by different manufacturers and at different locations. To pinpoint the physical origin of the heterogeneous SP, we investigated different conditions such as HOPG type, relative humidity (RH), and time after cleaving. Understanding this effect better could also provide a way to control or minimize it. Here, we reconcile the two opposite conclusions in the debate started by Lu *et al.*, by realizing the role of rotational effects and twisted graphene layers, which are now an intensive research topic. Our findings are valuable for the research communities for which HOPG is considered an ideal homogeneous system, like in scanning probe microscopy and single-layer graphene isolation. Particularly, KPFM users need to establish a more robust protocol for referencing their SP levels to a reliable standard, and should also shed some light on a still not fully understood material such as few-layers graphene.

2. Materials and methods

The HOPG substrates were B-Grade (Natural Kish Graphite Grade 200) with a nominal grain lateral size of 1 μm and $0.8^\circ \pm 0.2^\circ$ mosaic spread. The graphite sample surface was prepared by cleavage of the top layer with adhesive tape. To minimize the sample's thermal deformation, a graphite crystal of small dimensions 10 x 10 x 2 mm^3 was used. Different HOPG samples were measured with an AIST-NT Omegascope, an NT-MDT NTEGRA, and an Asylum Research MFP-3D AFM. The experiments were done in rooms with controlled humidity. We used Pt-coated probes from NT-MDT and AppNano (AccessEFM) with resonance frequencies of about 150 kHz and 70 kHz, respectively. If not stated differently, right after cleavage, HOPG was fast transferred to the AFM and continuously scanned to observe the SP's time-evolution. KPFM were measured in double-pass mode by an NT-MDT NTEGRA and an AIST-NT Omegascope AFM. In the first pass, the tip oscillated in amplitude-modulation (*i.e.*, tapping mode) to measure the surface topography, and in the second pass, the tip was lifted a given ΔH (in this work, ΔH was 10 nm or 20 nm). During this second pass, the tip was driven at the same resonance frequency as during the first pass, yet by electrical means, *i.e.*, by applying an AC bias. The contact potential difference (CPD) between tip and sample was obtained by applying a bias voltage to nullify the cantilever oscillation amplitude of first-order harmonic frequency. The SP is the sum resulting from different contributions, namely the CPD in conductive material – related to the tip and sample work functions, and possible electrostatic charges on the sample surface – likely due to dielectric domains or contamination. When an external potential V is established between the tip and the sample, an electrostatic force arises given by:

$$F_{\omega_{AC}} = \frac{\partial C}{\partial z}(V_{DC} - V_{CPD})V_{AC}sin(\omega_{AC}t) \quad (1)$$

To measure the SP, the V_{DC} is adjusted by the feedback loop of the AFM to nullify the amplitude of the cantilever's first-order harmonic. This nulling of the electrostatic force is reflected in eq. (1). The only way this term can be minimized is when V_{DC} equals V_{CPD}. Under this condition, the value V_{DC} is registered to express V_{CPD} or SP.

Horiba Labram HR Evolution was used for Raman measurements (laser power 25 mW, excitation energy 2.33 eV, acquisition time 1s and one accumulation, objective x100 and grating 1800) were done under an AFM (AIST-NT Omegascope) with the AFM probe retracted from the field of view in order to avoid any effect of the probe on the obtained spectra. KPFM maps of the same sample areas were measured both prior to and after Raman maps. Due to the retraction of the KPFM probe during Raman mapping, the mismatch between KPFM and Raman maps was tested on patterned samples and determined to be less than 2 μm in both x and y directions.

The KPFM measurements at different RH were conducted with an Asylum Research MFP-3D AFM. The EFM experiments were done in double-pass mode by an NT-MDT NTEGRA with constant V_{DC}. The lithography on HOPG was done by the NT-MDT NTEGRA with V_{DC} of 5 V in semi-contact mode.

3. Results and discussion

3.1. Domains observed in SP and hyperspectral Raman spectroscopy imaging

HOPG can be considered as a close relative of single-layer graphene. Individual graphene layers are held together in HOPG by relatively weak van der Waal forces, while the atoms within the layers are strongly bound within a hexagonal lattice by covalent bonds as illustrated in Fig. 1a. Hence, HOPG can be seen as a continuous vertical stack of an infinite number of graphene layers with strong spatial anisotropy. This anisotropy is reflected in the properties of HOPG, single-layer graphene, and other layered materials that define two orthogonal directions, in-plane and out-of-plane. When HOPG is observed from the top, the translational symmetry expected in this system dictates that all points are equivalent, and the surface should be homogeneous. In reality, this translational symmetry is broken by steps and grain boundaries in HOPG (see the topography in Fig. 1b). This broken symmetry can be the reason why we observe the big left and right domains in Fig. 1c. Apart from these 1D defects on the 2D basal planes, no differences are expected in HOPG. However as shown in the SP images, the domains marked by blue arrows are still observed in Fig. 1c. This can be related to dislocation beneath the surface of HOPG, which has been shown before by Tsuji and Yamanaka [19]. As we discuss below, these domains are reproducible.

Since Nonnenmacher *et al.* first introduced KPFM in 1991 [20], this method attracted great interest in surface science and makes it possible to characterize the electrical properties of materials at the nanoscale in terms of SP. For electrically conductive (properly-biased) and contaminant-free surfaces, this SP represents the CPD or the work function difference between conducting probe and sample when they are in contact. In electrically insulating materials or semiconductors, the buildup of static charges contributes to the SP contrast observed with KPFM [21].

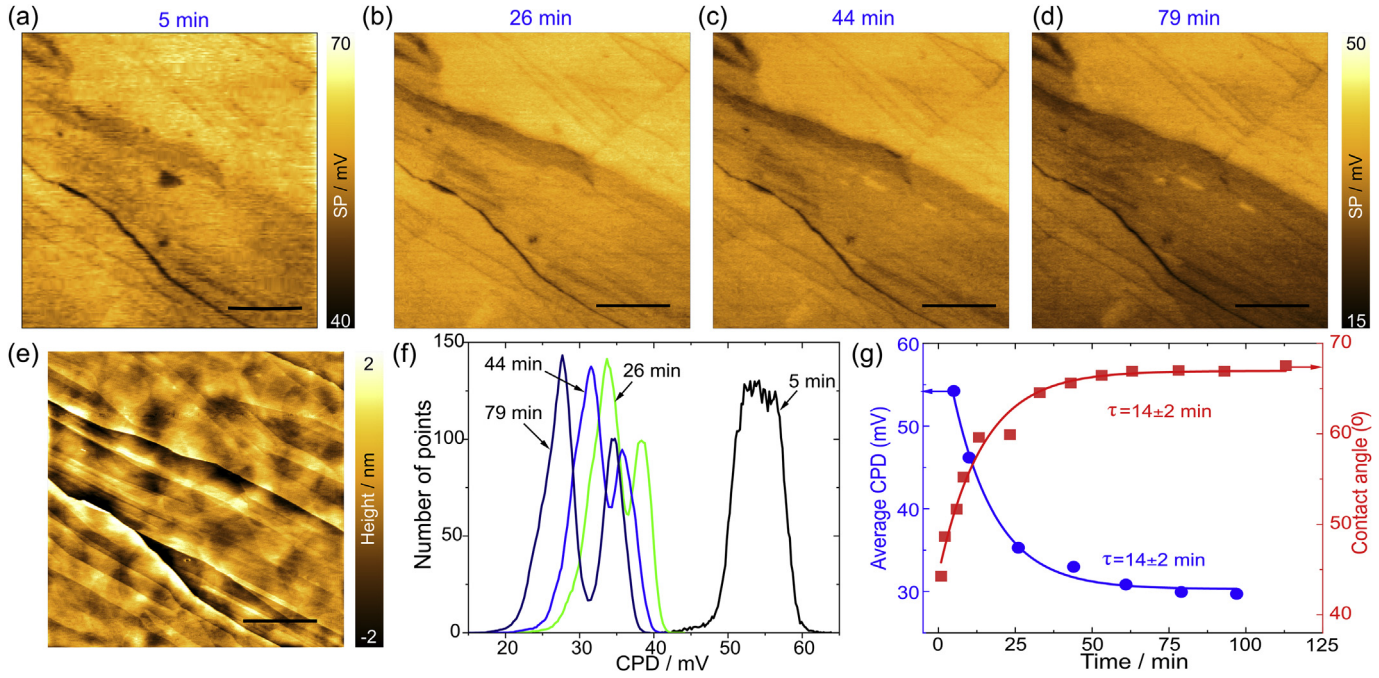

Fig. 1. (a) Schematic representation of HOPG. (b) Topography and (c) SP image images of HOPG. Arrows in (c) are highlighting electronic heterogeneities, in addition to the effects arising from the edges that are also visible in (b). The scale bar in all images is 5 μm. (A colour version of this figure can be viewed online.)

One of the major sources of surface modification in ambient conditions is the hydrocarbons in the environment. Thus, to verify the hypothesis of adsorption of environmental water and/or hydrocarbons, HOPG was freshly cleaved and quickly (within a few minutes) transferred to the AFM device to carry out the KPFM measurements. Typical SP images at different times are presented in Fig. 2, with the time indicating the elapsed period from the moment HOPG was cleaved. We observe that the SP images evolve over time. Initially, the electrical potential of HOPG is roughly uniform, then a typical domain with negative contrast appears. Then, the contrast progressively increases until it roughly stabilizes after 1 h. This time-dependent behavior points to the adsorption of airborne contaminants along with water on HOPG. It should be noted that, as in our case, the sample was prepared in the air, so airborne adsorption is inevitable as shown by Li *et al.* [22]. Initially, we suspected that the domains were the result of sample modification by the AFM tip. To investigate that possibility, we scanned the same region in KPFM mode for over 1 h and then zoomed out to look for any tip-induced contrast on the previously scanned area. We did not observe any significant tip-induced modification confirming that the effect shown in Fig. 2, even if correlated with time, is not due to tip-sample interaction. Contributions to the SP contrast due to tip contamination affect the SP due to changes in the tip work function but not the contrast among different domains. This is because when comparing different domains, we analyze the differences in SP and thus whatever tip changes occur they cancel out (see equation 3 in Supporting Information).

The SP distribution at different times of the images shown in Fig. 2a–d is presented in Fig. 2f. The bimodal distribution emerged at intermediate times (26, 44, and 79 min), leaving a single-peak distribution at 5 min. Lu *et al.* did not report the time evolution of the potential domains [16]. It is possible that in their case, as often happens in AFM, the image acquisition speed was too slow, requiring such a long time that only the asymptotic steady-state condition was recorded. In Fig. 2g, we present our SP together with the water contact angle reproduced from Lu and coworkers

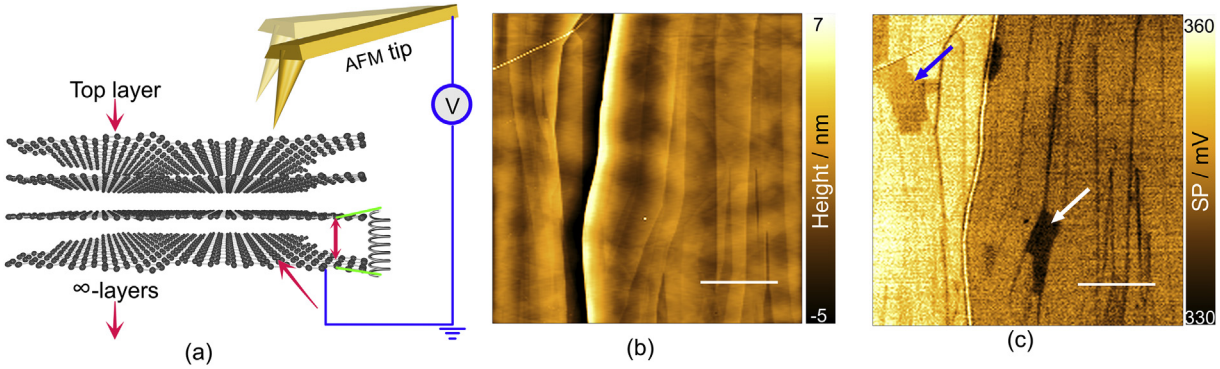

Fig. 2. Time evolution of SP images at a) 5 min, b) 26 min, c) 44 min, and d) 79 min after cleavage. e) Topography image of the sample. f) SP distributions at different times. g) Time dependence of average SP (blue circles) and water contact angle (red squares, adapted from Ref. [22]). The scale bar in all images is 5 μm. (A colour version of this figure can be viewed online.)

[22] as a function of time. We see that the average SP decreases over time, but becomes stable after about 1 h. For freshly-cleaved HOPG, the surface exhibits hydrophilic behavior. However, after adsorbing airborne species, the hydrophilicity of HOPG decreases [22]. The two processes have the same time constant of $\tau_{CA} \approx \tau_{SP} = 14 \pm 2$ min, fitted with a decay curve $y = A \cdot exp(-x/\tau) + y_0$. The obtained result is in agreement with the work function of HOPG changing due to hydrocarbon adsorption [23,24]. A similar time-evolution as that one shown in Fig. 2 was observed in the SP images using different setups at different laboratory locations (Russia and Austria) with different AFM instruments and different HOPG grades (see Fig. S1 in the supplementary information (SI)). This inter-laboratory analysis supports our conclusion that the effect of hydrocarbon adsorption on HOPG is inevitable and universal. Airborne hydrocarbons are supposed to be present everywhere, even in ultra-clean laboratory environments [25]. Many efforts were made to identify the airborne structure adsorbed on the surface of 2D materials, including analyses with X-ray photoelectron spectroscopy (XPS), Fourier-transform infrared spectroscopy (FTIR), tip-enhanced FTIR, force measurements, *etc.* [22,26,27]. Based on XPS results, Ashraf and coworkers observed that different hydrocarbons are adsorbed on the surface of HOPG, such as CH groups and carbon-oxygen functionalities such as carbonyl, carboxylic, and phenolic groups [26]. By using silicon gel sampler and gas chromatography coupled to a mass spectrometer operated in full scan and metastable ion monitoring mode, Illing *et al.* defined additional potential airborne contaminants in laboratory environments, including chelanthenes, phytanes, diocholestanes, hoptanes and hopanes [28]. Despite the above-shown evidence of the presence of hydrocarbon contaminants on HOPG, identifying the exact species is challenging because they are easily removed in the measurement due to their weak interaction with the substrate [27].

We also investigated the impact of water on the surface potential of HOPG (see Fig. S2). The average SP increases with the RH decrease. However, we did not observe a significant change in domains in SP images, despite the significant decrease in RH. Given that the SP domains on HOPG appear due to airborne contamination change over time, it remains to be explained why the adsorption is not the same everywhere but occurs differently at specific regions. It is well-known that there are defects on HOPG known as superlattices, which were discovered by several groups since the late 1980s [29,30]. Superlattices in HOPG can be produced by mechanical exfoliation with adhesive tape and are an intrinsic part of the cleaved surface [31,32]. Wong and Durkan found that mismatch and misorientation create superlattice domains with different periodicity in HOPG, which were visible by STM [33]. Hexagonal periodicities arise due to Moiré patterns related to superlattice and domains in HOPG with a rotational mismatch [32,34]. Since Raman spectroscopy is the tool of choice for investigating graphene and carbon-based materials, we expected that the mismatch angle between top layers and graphene layers underneath should be visible in the Raman spectra, thanks to the sensitivity of the technique to perturbations in graphene electronic structure. For this reason, we carried out a colocalized KPFM and Raman hyperspectral imaging analysis.

The results presented in Fig. 3 show a clear spatial overlap between the SP image and the Raman map of the G peak area. Whereas these two methods are completely independent of each other, the clear correlation observed here shows that the SP domains' location on the HOPG surface is not random. The SP domains clearly occur at specific locations with particular structural properties. The SP domains are not visible in the topography image in Fig. 3a; therefore, they must arise from defects beneath the sample surface. From the Raman spectrum in Fig. 3e, we see a blue shift in the G band from 1581.5 cm^{-1} to 1583.3 cm^{-1}. According to Wang *et al.*, this shift can be connected to the number of upper layers on HOPG [35]. However, the G band intensity at the point labeled 2 is lower than the intensity at point 1. The G band originates from optical phonons near the Γ point at the center of the Brillouin zone, with the in-plane stretching vibration of carbon atoms. The 2D band of bilayer graphene originates by the light activation of double-resonance processes from K to K′ point in the Brillouin zone. Because of the interaction between graphene layers, this system's electronic structure changes according to the number of AB-stacked graphene layers, which leads to different 2D peak shapes in the Raman spectrum. For monolayer graphene, there is one valence band and one conduction band in the Dirac cone; therefore, the 2D peak of graphene can be fitted by one Lorentzian peak. In the case of bilayer graphene, there are two conduction bands and two valence bands in bilayer graphene (parabolic bands at the K and K′ points), thus there are 4 electron-phonon interaction processes P_{11}, P_{12}, P_{21}, P_{22} in this system. The Raman modes associated to these four processes are then fitted by four Lorentzian peaks: ω_{11}, ω_{12}, ω_{21}, ω_{22}, respectively [36]. The 2D band of HOPG is not under debate; it is universal for all sp^2 carbon systems; it is accepted to be composed of two Lorentzian peaks that originate from the combination of an infinite number of peaks. For the case of HOPG, we cannot assume four peaks except for the P_{11} mode because of a strong singularity at ω_{11}. The second-order double-resonance process that is strongly affected by the stacking order or any other external perturbation allows the 2D peak to be used to identify the number of layers in graphene [37,38]. Similarly to the heterogeneous SP contrast, this Raman imaging result is unexpected since the spectral response of HOPG should be uniform. According to the Raman spectral analysis in Fig. 3e, the 2D band in HOPG has the same shape as bulk HOPG [39] with only two peaks at 2677.5 and 2720.4 cm^{-1}, and there are four peaks at point 2, assigned to 2640.8, 2691.1, 2720.1 and 2735.3 cm^{-1}. The 2D peak shape at point 2 describes the mixed character of bilayer graphene with bulk graphite as we observe the same peak at 2720 cm^{-1}. In comparison with the Raman spectrum of bilayer graphene reported previously [36], there is a blue shift in our Raman spectrum with Raman peaks P_{11}, P_{12}, and P_{21} and a red shift for P_{22}, this could be related to the impact of the bulk HOPG substrate under the twisted layers. The blue shift in misoriented bilayer graphene was reported before by Poncharal *et al.* [40], Hao and coauthors also showed the blue-shift in folded four-layer graphene in comparison with AB-stacking bilayer graphene [41]. The result obtained at location 2 is consistent with the presence of a decoupled bilayer-like graphene on HOPG. This conclusion is also justified by considering other factors that could affect the 2D band. These factors include doping, temperature, and mechanical stress. However, none of those factors affect the 2D peak shape but rather the peak intensity ratios and peak positions. Like with the 2D peak shape of bilayer graphene, characterized by a fit with four peaks related to the doubling of conduction and valence bands near the K and K′ points, four peaks provide the best fit to the spectrum we recorded for location 2.

We attribute the origin of decoupled bilayer-like graphene on HOPG to the mismatch angle between top graphene layers and bulk graphite that occurs during exfoliation. According to Ref. [42], the 1 + 1 folding graphene with large angle orientation has a Raman spectrum similar to that of monolayer graphene at a large mismatch angle. Based on *ab initio* and tight-binding calculations, Trambly de Laissardière *et al.* demonstrated a renormalization of electron velocity in bilayer graphene that depends on the rotational angle θ (RA) [43]. For large RA (15°−30°), the Fermi velocity of bilayer graphene is very close to that of monolayer graphene [44]. Shallcross *et al.* demonstrated that the electronic structure of bilayer and symmetric trilayer graphene with large RA at the K

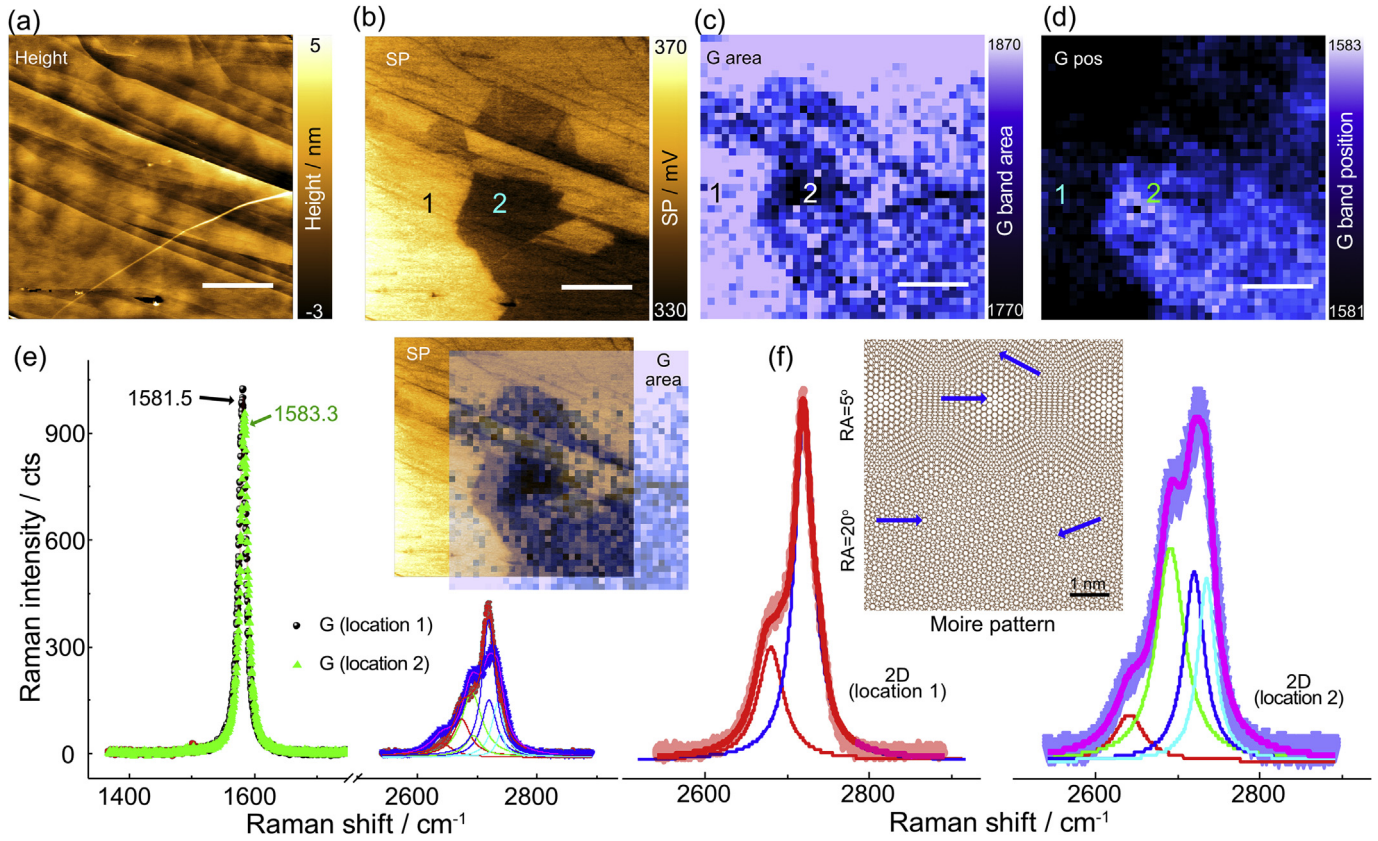

Fig. 3. Correlation between KPFM and Raman spectroscopy map: a) Topography, b) SP image, c) Raman map of G peak area, d) Raman map of G peak position, e) Raman spectrum at point 1 and 2 (marked in b). Inset of (e) presents an overlap of SP and G peak area images, f) Raman spectrum of 2D peak at point 1,2 and typical Moiré pattern at RA of 5° and 20°, the arrows point to the adsorption center. The scale bar in all images is 5 μm. (A colour version of this figure can be viewed online.)

point is similar to monolayer graphene [45], and the electronic structure at the K point is responsible for the 2D peak in the Raman spectrum of graphite. This also means that the large momentum mismatch around K–K′ points between the two graphene layers results in their electronic decoupling [46]. Luican *et al.* showed that when the mismatch angle between graphene layers is greater than 20°, the layers decouple, and the electronic properties of twisted bilayer graphene are indistinguishable from that of monolayer graphene [47]. Moreover, the spectrum of a folded tetralayer (2 + 2) graphene, in which one graphene bilayer is on top of another bilayer with a large RA of 29°, is similar to that of AB-stacked bilayer graphene obtained by mechanical exfoliation [48]; at this angle the top bilayer graphene most likely becomes decoupled from the bottom bilayer graphene. All these observations in the literature support our hypothesis of decoupled graphene-like layers on top of HOPG due to the mismatch angle of bilayer-like graphene with bulk HOPG. Although this is a dynamic topic still evolving, the consensus to explain the Moiré pattern on HOPG observed by STM is attributed to the mismatch angle between top graphene layers and bulk graphite [33,49,50]. Besides STM, Boi *et al.* recently used high-resolution transmission electron microscopy to show the presence of Moiré patterns on HOPG-lamellae exfoliated from bulk HOPG [51]. Thus, we based our conclusions on the Raman analysis and the general agreement about Moiré patterns as twisted graphene layers in HOPG as discussed above. This result is consistent with the possible presence of a defect (dislocation) under the top surface of HOPG, where few isolated graphene layers appear on the top of bulk HOPG [33]. To confirm our hypothesis, we used KPFM to measure natural kish graphite single crystals. As we expected from our deductions, we did not observe any SP domains (see Fig. S3) because of the almost perfect graphene structure. The fact that in our experimental results Raman spectroscopy was only sensitive to the topmost graphene layers of HOPG is surprising, as this is not a surface-sensitive technique such as XPS or KPFM. Although at this point, the details on the origin of this enhanced surface sensitivity in our Raman spectroscopy results are still elusive, we are tempted to attribute this to the appearance of van Hove singularities (vHs) [52]. Indeed, vHs appear in HOPG due to the strong coupling between the top graphene layers and the bulk substrate, as previously reported in an STM study [53]. Zhang and Luo showed that these vHs in HOPG display higher Fermi velocity and larger interlayer hopping than for the case of bilayer graphene. Like in the case of carbon nanotubes investigated by Saito *et al.* [54], vHs directly impact the joint density of states which would be visible in the Raman spectra as a resonance effect, amplifying the Raman signal from the top layer. This resonance due to vHs should be larger than the resonance arising from π-π* transitions from graphene layers in the bulk HOPG around the K and K' points of the Brillouin zone [55]. Moreover, from the Raman spectra image of the G peak, we see that not everywhere the layers appear with a large peak area. This could be related to the rotation-dependency of the optical transition energies, spanning the whole visible spectral range in twisted graphene as shown by tight-binding and DFT calculation results [56]. In addition to vHs, recently, Hu *et al.* showed that light can be confined in the gap between layers at the so-called magic angle, impacting the electronic properties [57]. As mentioned above, the Raman spectrum at location 2 has mixed characteristics of bilayer graphene and bulk HOPG. To isolate the spectrum of top bilayer-like graphene we need to subtract the bulk spectrum, assumed for location 1, from that of the bulk + bilayer at location 2. However, for

that analysis, we need the same bulk contribution for both locations so that one can serve as the reference and subtract it from the other location. But in our results, this same bulk contribution assumption may not be entirely correct because a larger photon absorption of the bilayer-like graphene in location 2 (*i.e.,* resonances due to van Hove singularities [52] and other factors discussed below) implies that fewer photons will reach the bulk graphite than in location 1. Therefore, the contribution from the bulk HOPG to the Raman spectra is different for both locations in Fig. 3e (and Fig. S4a). As can be seen from the subtraction after normalization in Fig. S4b, we have a resulting spectrum in region 2 that cannot be attributed to the "real" spectrum of top bilayer-like graphene. By taking into account the different bulk contributions for each region, we can obtain a subtraction result that matches that of bilayer-like graphene. This is shown in Fig. S4c, where the bulk contribution assumed for location 1 was scaled down to 0.4 times the bulk contribution for location 2. We notice that this factor of 0.4 is arbitrary, and we only use it to illustrate how scaling down the bulk contribution affects the subtraction result. In Fig. S4d, we show the Raman spectra for both regions and a sketch illustrating the different Raman laser penetration depths that make up different bulk contributions. Coming back to our resonance hypothesis, this implies that Raman imaging at different excitation wavelengths will make visible different domains due to resonance Raman spectroscopy that excites regions matching electronic transitions introduced by the twisted bilayers. Besides experiments, recent theoretical works show the opening of a bandgap due to the coupling between graphene bilayers [58]. We hope that our work will motivate rigorous theoretical modeling of graphene layers coupled to HOPG to provide additional insights into optical resonances in this system. We notice other factors that could contribute to the enhanced surface sensitivity in our Raman spectroscopy results. In addition to resonance conditions, another factor is the Raman scattering cross-section that for the coupled bilayer-like/HOPG system could be much larger than that of bulk HOPG. The chemical enhancement mechanism (graphene-enhanced Raman spectroscopy) [59,60], could also enhance the signal of the twisted bilayer-like graphene itself. It is also entirely possible that there is no enhancement of the top layer but that the twisted graphene is not restricted to the top layers and goes deeper inside HOPG, explaining why we get a considerably larger Raman signal in location 2 that resembles a graphene-like bilayer. At present, our knowledge on the spatial extension of rotational defects inside HOPG is quite limited; further investigations with colocalized low-energy electron microscopy (LEEM) and Raman microscopy could shed light on this question.

It is reasonable to expect that the misorientation of graphene layers affects the van der Waals interaction between the top of graphene superlattice and airborne matter in the environment. This situation gives rise to locations on HOPG that are more attractive than others towards airborne adsorption, leading to a locally low SP. Xhie *et al.* used STM to investigate the adsorption of cobalt atoms on HOPG. They showed that Co nanoparticles or clusters (atoms) are preferably adsorbed on locations with the highest density of states at the Fermi level with AA stacking [61]. Besides that, Balog and coauthors proved that hydrogen adsorption follows the Moiré pattern of graphene on Ir(111) [62]. Adsorption of organic molecules such as perylene-3,4,9,10-tetracarboxylic dianhydride, phthalocyanine (and its metal coordination complexes), and C_{60} fullerenes, also follows this behavior [63]. In the case of fullerenes, C_{60} molecules are preferably adsorbed on the valleys of Moiré patterns [64]. This can be understood by considering that the larger the relative RA between HOPG top layers, the smaller the lattice periodicity. As the RA increases, the lattice period decreases and the valley's density increases. Thus, the larger density of adsorption centers increases hydrocarbons' concentration and airborne organics adsorbed on HOPG. All experiments discussed above were done at the nanoscale, but also at larger scales, islands and domains of melamine self-assembled monolayers on HOPG were also observed [65]. In summary, due to the higher adsorption of hydrocarbons on superlattices with lower periodicity (higher relative RA), the SP values of these superlattices are lower than for other regions and this is why we observe domains with different SP in KPFM imaging.

3.2. Effect of applied potential to hydrocarbon adsorption

Inspired by observing inhomogeneous contrast in electric force microscopy (EFM) images reported by Lu and co-workers [16], we performed EFM of HOPG and correlated it with KPFM results obtained on the same sample under the same experimental conditions. We expected to see in EFM the same contrast – including domains – that we saw in KPFM for freshly-cleaved HOPG. For EFM, we utilized the same tip used in KPFM, with a DC voltage of 1 V and lift height (dZ) of 20 nm. However, our results in Fig. 4c revealed no domains like in Fig. 4b.

We assume that the SP domain contrast with the surrounding HOPG at 3 h after cleavage is as small as 30 mV. By applying a DC voltage of 1 V, the difference in electric force due to the possible presence of domains is relatively low, so we can hardly detect the domains in the EFM image. Indeed, the phase image in Fig. 4d is almost homogenous without the clear appearance of any domain. This result contrasts with that of Lu's work, in which they applied 3 V and still observed the domains [16]. However, after exposure to air for one day, we observed the domain in the phase and EFM images (see Figs. S5b and S5c) like in Lu and co-workers' report. Therefore, the time of measurement since cleavage appears to be critical. If the sample is left in the air for 1 day, we observe a strong correlation among SP, phase, and topography images obtained with KPFM (see Fig. 5a–c). This correlation indicates the water/hydrocarbon adsorption layers that define the domains on HOPG (in particular, the phase-contrast that is sensitive to the sample's adhesive properties) [66,67]. In freshly cleaved HOPG we do not see this correlation because the layer of adsorbed hydrocarbons is too thin to be appreciated. For HOPG left exposed to air for an extended period (1 day), we discovered that hydrocarbons adsorbed on HOPG could be removed by applying a potential difference during EFM scanning. After multiple EFM scans using 2 V, 0.3 A, and 20 nm dZ, the domains on the surface gradually disappeared. After changing to KPFM mode to observe the effect of scanning under bias, we found that the adsorbed layers were removed during EFM imaging, as evidenced by the topography and phase images in Fig. 5d–f.

A part of the domain previously observed in SP images disappeared after EFM, and the average SP increased. The phase images in Fig. S5 showed that most of the hydrocarbons were removed. We can still see the domain in the SP image, which can be explained because it took 20 min for the KPFM scan to be completed, and during that time airborne hydrocarbons were adsorbed back to the surface (see Fig. S6). This re-adsorption is even evident on a single scan frame from bottom to top, matching the scan direction and increasing SP contrast. After 9 h exposure to air, the domains in SP images reappeared (see Fig. 5g–i). These observations provide additional evidence of the effect of airborne adsorption on the SP image. Therefore, we demonstrated that, as opposed to conclusion by Lu and coworkers [16], large contrast changes and domains in SP in HOPG appear due to airborne adsorption and not because of intrinsic SP of defects in HOPG. The impact of applied potential is confirmed by lithography with an applied voltage of 5 V in semi-contact mode (see Fig. S7). The KPFM results for that sample showed that the external potential entirely

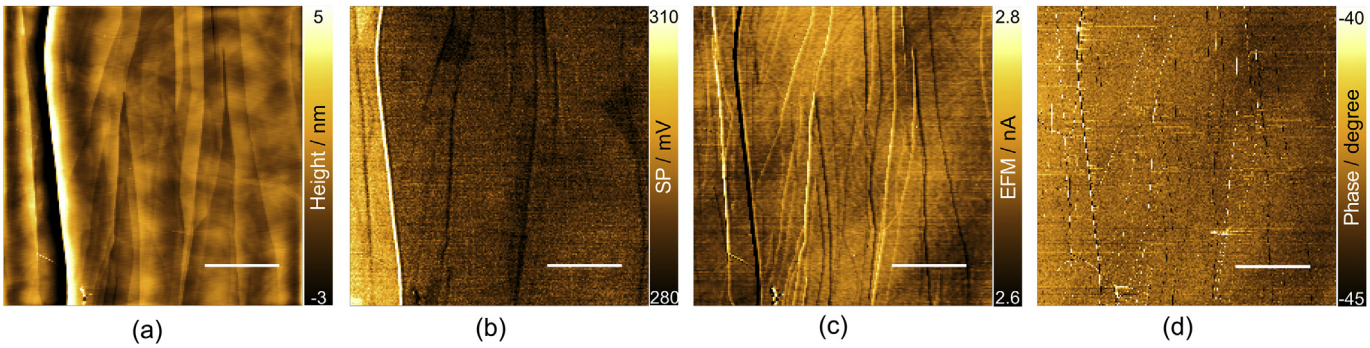

Fig. 4. Typical (a) topography, (b) SP, (c) EFM image (applied voltage: 1 V), and (d) phase, 3 h after cleavage. The scale bar in all images is 5 μm. (A colour version of this figure can be viewed online.)

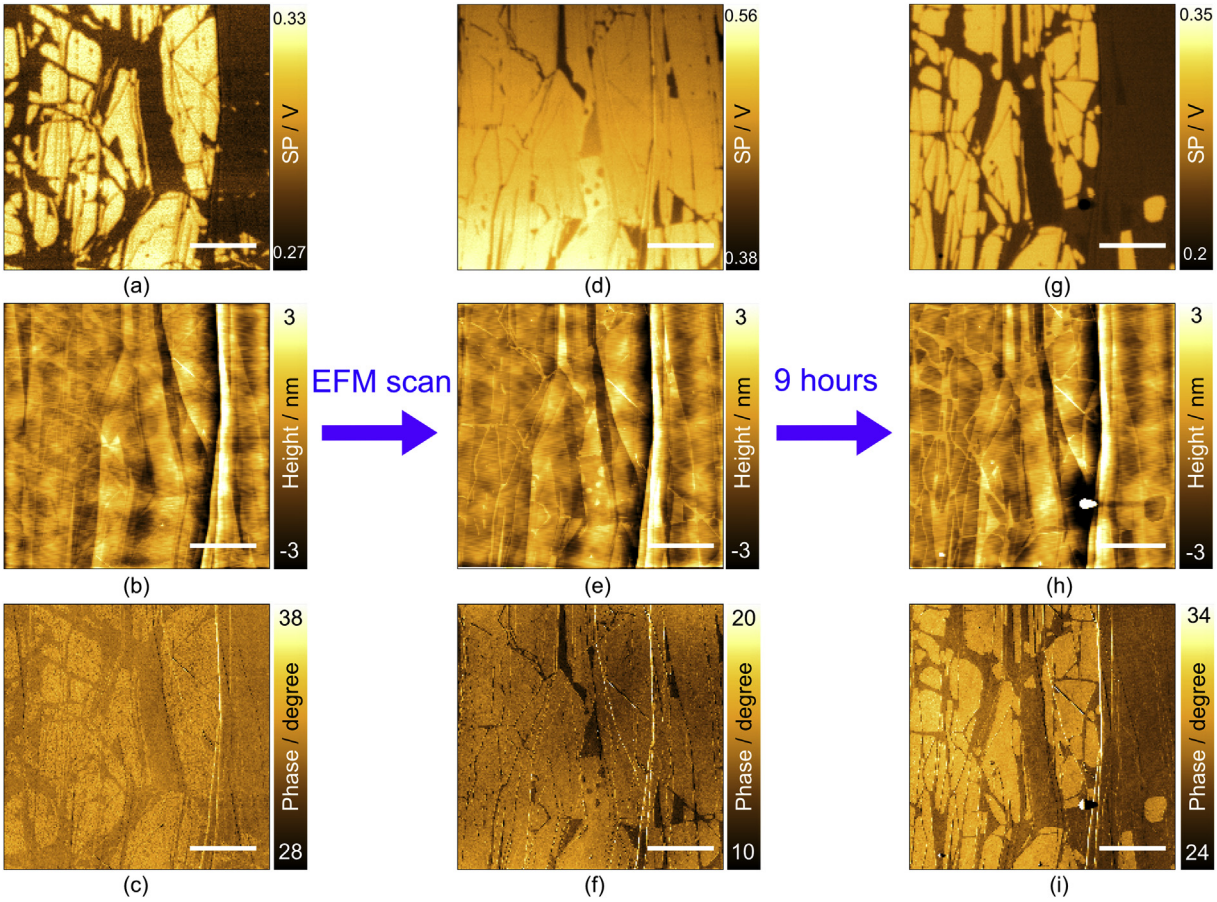

Fig. 5. EFM effect on hydrocarbon adsorption on HOPG, a) SP image, b) topography, c) phase image of old HOPG before EFM; d) SP image, e) topography, f) phase image of old HOPG after EFM; g) SP image, h) topography, k) phase image of old HOPG after 9 h. The scale bars are 5 μm. (A colour version of this figure can be viewed online.)

removed hydrocarbons. This demonstrates the viability of a nanoscale way for *in situ* removal of airborne species adsorbed on HOPG compared with traditional thermal annealing or UV/O_3 treatment.

Additional experimental work with the *in situ* combinations of different surface-sensitive methods will shed light on the many questions about this carbon system that still elude us. Here are some of those open questions that are also interrelated: Are the twisted graphene layers restricted to the top 1–2 layers? Or do they propagate deeper inside HOPG? If yes, how deep? What is the impact of the top layers/HOPG coupling to the phonon and electronic properties? We are now aiming to answer these questions, particularly with the combination of STM and tip-enhanced Raman spectroscopy [68]. We hope that our work will motivate rigorous theoretical modeling of graphene layers coupled to HOPG and provide evidence on the existence of optical resonances in this system that, if true, could also have implications in optoelectronics.

4. Conclusion

Employing KPFM, we systematically investigated the presence of SP domains in HOPG and revealed that their physical origin is related to the formation of defects as rotationally miss-matched domains, *i.e.*, twisted graphene layers in graphite. We showed that the time evolution of these domains is due to hydrocarbon

adsorption, which is in contrast to the hypothesis of Lu *et al.* [16]. The time after cleavage is critical to investigate the physical and chemical properties of HOPG: at ~60 min after cleavage, the SP image contrast stabilizes, which is consistent with the impact of hydrocarbon adsorption to time-dependent water contact angle results by Li and co-workers [22]. Moreover, Raman hyperspectral imaging proved that the formation of domains is not random, but these domains are formed because hydrocarbons are preferably adsorbed on the defects, which is most likely due to a high mismatch angle between the top graphene layers and the bulk. The larger relative RA, the smaller the periodicity of Moiré pattern and the higher the density of adsorption centers. Therefore, more hydrocarbons are adsorbed on these defects. Besides, the adsorbed hydrocarbons can be effectively removed by establishing a tip-sample bias during scanning, which also allows reproducing the time-dependent visualization of re-adsorbed hydrocarbons.

Upon mechanical stress, the top graphene layers of HOPG appear intrinsically separated from the underlying bulk. Since cleavage by adhesive tape is by far the most used way to process HOPG and is also very popular for graphene preparation, we foresee substantial implications of the present work for the self-assembly of organic molecules on HOPG, twisted graphene, and the emerging field of twistronics.

CRediT authorship contribution statement

Tuan-Hoang Tran: Investigation, Validation, Formal analysis, Visualization, Writing - original draft, Writing - review & editing, Project administration. **Raul D. Rodriguez:** Conceptualization, Methodology, Visualization, Supervision, Writing - original draft, Writing - review & editing, Funding acquisition. **Marco Salerno:** Conceptualization, Investigation, Validation, Formal analysis, Writing - original draft, Writing - review & editing. **Aleksandar Matković:** Investigation, Validation, Formal analysis, Visualization, Writing - original draft, Writing - review & editing, Funding acquisition. **Christian Teichert:** Writing - original draft, Writing - review & editing, Funding acquisition. **Evgeniya Sheremet:** Validation, Supervision, Writing - original draft, Writing - review & editing, Resources, Project administration.

Declaration of competing interest

The authors declare that they have no known competing financial interests or personal relationships that could have appeared to influence the work reported in this paper.

Acknowledgements

This work was funded by RFBR and FWF research project No. 19-52-14006. A.M. acknowledges the support by the Austrian Science Fund (FWF Der Wissenschaftsfonds) through project I4323- N36. This research is supported by the Tomsk Polytechnic University (TPU) within the framework of the Tomsk Polytechnic University Competitiveness Enhancement Program, 5–100. We are grateful to the TPU vicerector Prof. Mekhman Yusubov for support with the acquisition of the AFM/Raman setup. M.S. was supported for this work by the Statutory research project of the Department of Functional Materials and Hydrogen Technology of MUT. Infrastructural support (Raman-TERS laboratory) by Montanuniversität Leoben is acknowledged.

Appendix A. Supplementary data

Supplementary data to this article can be found online at https://doi.org/10.1016/j.carbon.2021.01.152.

References

[1] K.S. Novoselov, A.K. Geim, S.V. Morozov, D. Jiang, Y. Zhang, S.V. Dubonos, I.V. Grigorieva, A.A. Firsov, Electric field effect in atomically thin carbon films, Science 306 (2004) 666–669.
[2] H. Li, Q. Zhang, C.C.R. Yap, B.K. Tay, T.H.T. Edwin, A. Olivier, D. Baillargeat, From bulk to monolayer MoS2: evolution of Raman scattering, Adv. Funct. Mater. 22 (2012) 1385–1390.
[3] Y. Yang, H. Du, Q. Xue, X. Wei, Z. Yang, C. Xu, D. Lin, W. Jie, J. Hao, Three-terminal memtransistors based on two-dimensional layered gallium selenide nanosheets for potential low-power electronics applications, Nano Energy 57 (2019) 566–573.
[4] D.V. Demidov, I.P. Prosvirin, A.M. Sorokin, V.I. Bukhtiyarov, Model Ag/Hopg catalysts: preparation and STM/XPS study, Catal. Sci. Technol. 1 (2011) 1432, https://doi.org/10.1039/c1cy00127b.
[5] I.G. Grigorieva, A.A. Antonov, Hopg as powerful x-ray optics, X Ray Spectrom. 32 (2003) 64–68, https://doi.org/10.1002/xrs.617.
[6] T. Brülle, W. Ju, P. Niedermayr, A. Denisenko, O. Paschos, O. Schneider, U. Stimming, Size-dependent electrocatalytic activity of gold nanoparticles on Hopg and highly boron-doped diamond surfaces, Molecules 16 (2011) 10059–10077.
[7] A.M. Oliveira Brett, A.-M. Chiorcea Paquim, DNA imaged on a Hopg electrode surface by AFM with controlled potential, Bioelectrochemistry 66 (2005) 117–124.
[8] C.F. Blanford, F.A. Armstrong, The pyrolytic graphite surface as an enzyme substrate: microscopic and spectroscopic studies, J. Solid State Electrochem. 10 (2006) 826–832, https://doi.org/10.1007/s10008-006-0183-2.
[9] V.Y. Yurov, V. Yu Yurov, A.N. Klimov, Scanning tunneling microscope calibration and reconstruction of real image: drift and slope elimination, Rev. Sci. Instrum. 65 (1994) 1551–1557, https://doi.org/10.1063/1.1144890.
[10] P.A. Fernández Garrillo, B. Grévin, N. Chevalier, Ł. Borowik, Calibrated work function mapping by Kelvin probe force microscopy, Rev. Sci. Instrum. 89 (2018), 043702.
[11] S. Rentenberger, A. Vollmer, E. Zojer, R. Schennach, N. Koch, UV/ozone treated Au for air-stable, low hole injection barrier electrodes in organic electronics, J. Appl. Phys. 100 (2006), 053701, https://doi.org/10.1063/1.2336345.
[12] B. Stadlober, U. Haas, H. Gold, A. Haase, G. Jakopic, G. Leising, N. Koch, S. Rentenberger, E. Zojer, Orders-of-magnitude reduction of the contact resistance in short-channel hot embossed organic thin film transistors by oxidative treatment of Au-electrodes, Adv. Funct. Mater. 17 (2007) 2687–2692.
[13] J. Červenka, M.I. Katsnelson, C.F.J. Flipse, Room-temperature ferromagnetism in graphite driven by two-dimensional networks of point defects, Nat. Phys. 5 (2009) 840–844, https://doi.org/10.1038/nphys1399.
[14] M. Salerno, S. Dante, Scanning Kelvin probe microscopy: challenges and perspectives towards increased application on biomaterials and biological samples, Materials 11 (2018), https://doi.org/10.3390/ma11060951.
[15] R. Proksch, Multifrequency, repulsive-mode amplitude-modulated atomic force microscopy, Appl. Phys. Lett. 89 (2006) 113121.
[16] Y. Lu, M. Muñoz, C.S. Steplecaru, C. Hao, M. Bai, N. Garcia, K. Schindler, P. Esquinazi, Electrostatic force microscopy on oriented graphite surfaces: coexistence of insulating and conducting behaviors, Phys. Rev. Lett. 97 (2006), 076805.
[17] S. Sadewasser, T. Glatzel, Comment on "electrostatic force microscopy on oriented graphite surfaces: coexistence of insulating and conducting behaviors, Phys. Rev. Lett. 98 (2007) 269701, discussion 269702.
[18] Y. Lu, M. Munoz, C.S. Steplecaru, C. Hao, M. Bai, N. Garcia, K. Schindler, D. Spoddig, P. Esquinazi, Lu, et al., Reply: Phys. Rev. Lett. 98 (2007) 269701.
[19] T. Tsuji, K. Yamanaka, Observation by ultrasonic atomic force microscopy of reversible displacement of subsurface dislocations in highly oriented pyrolytic graphite, Nanotechnology 12 (2001) 301–307, https://doi.org/10.1088/0957-4484/12/3/318.
[20] M. Nonnenmacher, M.P. O'Boyle, H.K. Wickramasinghe, Kelvin probe force microscopy, Appl. Phys. Lett. 58 (1991) 2921–2923, https://doi.org/10.1063/1.105227.
[21] S. Sadewasser, T. Glatzel, Kelvin Probe Force Microscopy: from Single Charge Detection to Device Characterization, Springer, 2018.
[22] Z. Li, Y. Wang, A. Kozbial, G. Shenoy, F. Zhou, R. McGinley, P. Ireland, B. Morganstein, A. Kunkel, S.P. Surwade, L. Li, H. Liu, Effect of airborne contaminants on the wettability of supported graphene and graphite, Nat. Mater. 12 (2013) 925–931.
[23] Y.-X. Yu, Binding energy and work function of organic electrode materials phenanthraquinone, pyromellitic dianhydride and their derivatives adsorbed on graphene, ACS Appl. Mater. Interfaces 6 (2014) 16267–16275.
[24] C. Sommerhalter, T.W. Matthes, T. Glatzel, A. Jäger-Waldau, M. Ch Lux-Steiner, High-sensitivity quantitative Kelvin probe microscopy by noncontact ultra-high-vacuum atomic force microscopy, Appl. Phys. Lett. 75 (1999) 286–288, https://doi.org/10.1063/1.124357.
[25] A. Kurokawa, K. Odaka, Y. Azuma, T. Fujimoto, I. Kojima, Diagnosis and cleaning of carbon contamination on SiO2 thin film, J. Surf. Anal. 15 (2009) 337–340.
[26] A. Ashraf, Y. Wu, M.C. Wang, N.R. Aluru, S.A. Dastgheib, S. Nam, Spectroscopic investigation of the wettability of multilayer graphene using highly ordered pyrolytic graphite as a model material, Langmuir 30 (2014) 12827–12836.

[27] Z. Peng, R. Yang, M.A. Kim, L. Li, H. Liu, Influence of O2, H2O and airborne hydrocarbons on the properties of selected 2D materials, RSC Adv. 7 (2017) 27048–27057, https://doi.org/10.1039/c7ra02130e.
[28] C.J. Illing, C. Hallmann, K.E. Miller, R.E. Summons, H. Strauss, Airborne hydrocarbon contamination from laboratory atmospheres, Org. Geochem. 76 (2014) 26–38.
[29] T.R. Albrecht, H.A. Mizes, J. Nogami, S. Park, C.F. Quate, Observation of tilt boundaries in graphite by scanning tunneling microscopy and associated multiple tip effects, Appl. Phys. Lett. 52 (1988) 362–364, https://doi.org/10.1063/1.99465.
[30] M. Kuwabara, D.R. Clarke, D.A. Smith, Anomalous superperiodicity in scanning tunneling microscope images of graphite, Appl. Phys. Lett. 56 (1990) 2396–2398, https://doi.org/10.1063/1.102906.
[31] H. Chang, A.J. Bard, Observation and characterization by scanning tunneling microscopy of structures generated by cleaving highly oriented pyrolytic graphite, Langmuir 7 (1991) 1143–1153.
[32] W.-T. Pong, C. Durkan, A review and outlook for an anomaly of scanning tunnelling microscopy (STM): superlattices on graphite, J. Phys. D Appl. Phys. 38 (2005) R329.
[33] H.S. Wong, C. Durkan, Unraveling the rotational disorder of graphene layers in graphite, Phys. Rev. B 81 (2010), https://doi.org/10.1103/physrevb.81.045403.
[34] A.H. MacDonald, R. Bistritzer, Materials science: graphene moiré mystery solved? Nature 474 (2011) 453–454.
[35] H. Wang, Y. Wang, X. Cao, M. Feng, G. Lan, Vibrational properties of graphene and graphene layers, J. Raman Spectrosc. 40 (2009) 1791–1796, https://doi.org/10.1002/jrs.2321.
[36] L.M. Malard, J. Nilsson, D.C. Elias, J.C. Brant, F. Plentz, E.S. Alves, A.H. Castro Neto, M.A. Pimenta, Probing the electronic structure of bilayer graphene by Raman scattering, Phys. Rev. B 76 (2007), https://doi.org/10.1103/physrevb.76.201401.
[37] L.M. Malard, M.A. Pimenta, G. Dresselhaus, M.S. Dresselhaus, Raman spectroscopy in graphene, Phys. Rep. 473 (2009) 51–87, https://doi.org/10.1016/j.physrep.2009.02.003.
[38] L.G. Cançado, A. Reina, J. Kong, M.S. Dresselhaus, Geometrical approach for the study ofG'band in the Raman spectrum of monolayer graphene, bilayer graphene, and bulk graphite, Phys. Rev. B 77 (2008), https://doi.org/10.1103/physrevb.77.245408.
[39] L.M. Malard, M.A. Pimenta, G. Dresselhaus, M.S. Dresselhaus, Raman spectroscopy in graphene, Phys. Rep. 473 (2009) 51–87, https://doi.org/10.1016/j.physrep.2009.02.003.
[40] P. Poncharal, A. Ayari, T. Michel, J.-L. Sauvajol, Raman spectra of misoriented bilayer graphene, Phys. Rev. B 78 (2008), https://doi.org/10.1103/physrevb.78.113407.
[41] Y. Hao, Y. Wang, L. Wang, Z. Ni, Z. Wang, R. Wang, C.K. Koo, Z. Shen, J.T.L. Thong, Probing layer number and stacking order of few-layer graphene by Raman spectroscopy, Small 6 (2010) 195–200.
[42] Z. Ni, Y. Wang, T. Yu, Y. You, Z. Shen, Reduction of Fermi velocity in folded graphene observed by resonance Raman spectroscopy, Phys. Rev. B 77 (2008), https://doi.org/10.1103/physrevb.77.235403.
[43] G. Trambly de Laissardière, D. Mayou, L. Magaud, Localization of Dirac electrons in rotated graphene bilayers, Nano Lett. 10 (2010) 804–808.
[44] E.S. Morell, E. Suárez Morell, P. Vargas, L. Chico, L. Brey, Charge redistribution and interlayer coupling in twisted bilayer graphene under electric fields, Phys. Rev. B 84 (2011), https://doi.org/10.1103/physrevb.84.195421.
[45] S. Shallcross, S. Sharma, O.A. Pankratov, Quantum interference at the twist boundary in graphene, Phys. Rev. Lett. 101 (2008), 056803.
[46] P. Rickhaus, M.-H. Liu, M. Kurpas, A. Kurzmann, Y. Lee, H. Overweg, M. Eich, R. Pisoni, T. Taniguchi, K. Watanabe, K. Richter, K. Ensslin, T. Ihn, The electronic thickness of graphene, Sci. Adv. 6 (2020), eaay8409.
[47] A. Luican, G. Li, A. Reina, J. Kong, R.R. Nair, K.S. Novoselov, A.K. Geim, E.Y. Andrei, Single-layer behavior and its breakdown in twisted graphene layers, Phys. Rev. Lett. 106 (2011) 126802.
[48] C. Cong, T. Yu, Evolution of RamanGandG'(2D) modes in folded graphene layers, Phys. Rev. B 89 (2014), https://doi.org/10.1103/physrevb.89.235430.
[49] H.-L. Sun, Q.-T. Shen, J.-F. Jia, Q.-Z. Zhang, Q.-K. Xue, Scanning tunneling microscopy study of superlattice domain boundaries on graphite surface, Surf. Sci. 542 (2003) 94–100, https://doi.org/10.1016/s0039-6028(03)00949-x.
[50] Y. Wang, Y. Ye, K. Wu, Simultaneous observation of the triangular and honeycomb structures on highly oriented pyrolytic graphite at room temperature: an STM study, Surf. Sci. 600 (2006) 729–734, https://doi.org/10.1016/j.susc.2005.12.001.
[51] F.S. Boi, G. Shuai, J. Wen, S. Wang, Unusual Moiré superlattices in exfoliated μm-thin Hopg lamellae: an angular-diffraction study, Diam. Relat. Mater. 108 (2020) 107920, https://doi.org/10.1016/j.diamond.2020.107920.
[52] G. Li, A. Luican, J.M.B.L. dos Santos, A.H. Castro Neto, A. Reina, J. Kong, E.Y. Andrei, Observation of Van Hove singularities in twisted graphene layers, Nat. Phys. 6 (2010) 109–113, https://doi.org/10.1038/nphys1463.
[53] X. Zhang, H. Luo, Scanning tunneling spectroscopy studies of angle-dependent van Hove singularities on twisted graphite surface layer, Appl. Phys. Lett. 103 (2013) 231602.
[54] R. Saito, A. Grüneis, G.G. Samsonidze, G. Dresselhaus, M.S. Dresselhaus, A. Jorio, L.G. Cançado, M.A. Pimenta, A.G. Souza Filho, Optical absorption of graphite and single-wall carbon nanotubes, Appl. Phys. A 78 (2004) 1099–1105, https://doi.org/10.1007/s00339-003-2459-z.
[55] A. Grüneis, R. Saito, G.G. Samsonidze, T. Kimura, M.A. Pimenta, A. Jorio, A.G.S. Filho, G. Dresselhaus, M.S. Dresselhaus, Inhomogeneous optical absorption around the K point in graphite and carbon nanotubes, Phys. Rev. B Condens. Matter 67 (2003) 13, https://doi.org/10.1103/PhysRevB.67.165402.
[56] A. Vela, M.V.O. Moutinho, F.J. Culchac, P. Venezuela, R.B. Capaz, Electronic structure and optical properties of twisted multilayer graphene, Phys. Rev. B Condens. Matter 98 (2018), https://doi.org/10.1103/PhysRevB.98.155135.
[57] G. Hu, Q. Ou, G. Si, Y. Wu, J. Wu, Z. Dai, A. Krasnok, Y. Mazor, Q. Zhang, Q. Bao, C.-W. Qiu, A. Alù, Topological polaritons and photonic magic angles in twisted α-MoO3 bilayers, Nature 582 (2020) 209–213, https://doi.org/10.1038/s41586-020-2359-9.
[58] F.J. Culchac, R.R. Del Grande, R.B. Capaz, L. Chico, E.S. Morell, Flat bands and gaps in twisted double bilayer graphene, Nanoscale 12 (2020) 5014–5020.
[59] X. Ling, L.G. Moura, M.A. Pimenta, J. Zhang, Charge-transfer mechanism in graphene-enhanced Raman scattering, J. Phys. Chem. C 116 (2012) 25112–25118, https://doi.org/10.1021/jp3088447.
[60] X. Ling, J. Wu, L. Xie, J. Zhang, Graphene-Thickness-dependent graphene-enhanced Raman scattering, J. Phys. Chem. C 117 (2013) 2369–2376, https://doi.org/10.1021/jp310564d.
[61] J. Xhie, K. Sattler, M. Ge, N. Venkateswaran, Giant and supergiant lattices on graphite, Phys. Rev. B Condens. Matter 47 (1993) 15835–15841.
[62] R. Balog, B. Jørgensen, L. Nilsson, M. Andersen, E. Rienks, M. Bianchi, M. Fanetti, E. Laegsgaard, A. Baraldi, S. Lizzit, Z. Sljivancanin, F. Besenbacher, B. Hammer, T.G. Pedersen, P. Hofmann, L. Hornekaer, Bandgap opening in graphene induced by patterned hydrogen adsorption, Nat. Mater. 9 (2010) 315–319.
[63] J.M. MacLeod, F. Rosei, Molecular self-assembly on graphene, Small 10 (2014) 1038–1049, https://doi.org/10.1002/smll.201301982.
[64] J. Lu, P.S.E. Yeo, Y. Zheng, Z. Yang, Q. Bao, C.K. Gan, K.P. Loh, Using the graphene Moiré pattern for the trapping of C60 and homoepitaxy of graphene, ACS Nano 6 (2012) 944–950.
[65] H.-M. Zhang, Z.-K. Pei, Z.-X. Xie, L.-S. Long, B.-W. Mao, X. Xu, L.-S. Zheng, Preparing self-assembled monolayers of cyanuric acid and melamine complex on Hopg surfaces, J. Phys. Chem. C 113 (2009) 13940–13946, https://doi.org/10.1021/jp903406q.
[66] A. Noy, C.H. Sanders, D.V. Vezenov, S.S. Wong, C.M. Lieber, Chemically-sensitive imaging in tapping mode by chemical force microscopy: relationship between phase lag and adhesion, Langmuir 14 (1998) 1508–1511, https://doi.org/10.1021/la970948f.
[67] R. García, Amplitude Modulation Atomic Force Microscopy, Wiley, 2010.
[68] E. Sheremet, R.D. Rodriguez, A.L. Agapov, A.P. Sokolov, M. Hietschold, D.R.T. Zahn, Nanoscale imaging and identification of a four-component carbon sample, Carbon 96 (2016) 588–593, https://doi.org/10.1016/j.carbon.2015.09.104.